Author's Accepted Manuscript

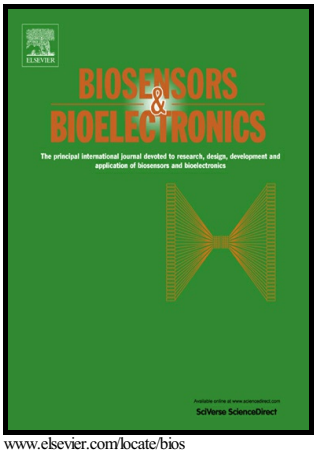

www.elsevier.com/locate/bios

A label-free cellulose SERS biosensor chip with improvement of nanoparticle-enhanced LSPR effects for early diagnosis of subarachnoid hemorrhage-induced complications

Wansun Kim, Sung Ho Lee, Yong Jin Ahn, Seung Ho Lee, Jiwook Ryu, Seok Keun Choi, Samjin Choi

PII: S0956-5663(18)30257-4
DOI: https://doi.org/10.1016/j.bios.2018.04.003
Reference: BIOS10399

To appear in: *Biosensors and Bioelectronic*

Received date: 9 February 2018
Revised date: 28 March 2018
Accepted date: 2 April 2018

Cite this article as: Wansun Kim, Sung Ho Lee, Yong Jin Ahn, Seung Ho Lee, Jiwook Ryu, Seok Keun Choi and Samjin Choi, A label-free cellulose SERS biosensor chip with improvement of nanoparticle-enhanced LSPR effects for early diagnosis of subarachnoid hemorrhage-induced complications, *Biosensors and Bioelectronic,* https://doi.org/10.1016/j.bios.2018.04.003

A label-free cellulose SERS biosensor chip with improvement of nanoparticle-enhanced LSPR effects for early diagnosis of subarachnoid hemorrhage-induced complications

Wansun Kim[a,1], Sung Ho Lee[b,1], Yong Jin Ahn[a], Seung Ho Lee[a], Jiwook Ryu[b], Seok Keun Choi[b], Samjin Choi[a]*

[a] Department of Biomedical Engineering, College of Medicine, Kyung Hee University, Seoul 02447, Republic of Korea

[b] Department of Neurosurgery, College of Medicine, Kyung Hee University, Seoul 02447, Republic of Korea

***Address for correspondence:** Samjin Choi, Ph.D., Department of Biomedical Engineering, College of Medicine, Kyung Hee University, 26, Kyungheedae-ro, Dongdaemun-gu, Seoul 02447, Korea. Tel: +82 2 961 0290, Fax: +82 2 961 5515, E-mail addresses: medchoi@khu.ac.kr

[1] **These authors contributed equally to this work.**

Abstract

It is very difficult to predict some complications after subarachnoid hemorrhage (SAH), despite rapid advances in medical science. Herein, we introduce a label-free cellulose surface-enhanced Raman spectroscopy (SERS) biosensor chip with pH-functionalized, gold nanoparticle (AuNP)-enhanced localized surface plasmon resonance (LSPR) effects for identification of SAH-induced cerebral vasospasm and hydrocephalus caused by cerebrospinal fluid (CSF). The SERS biosensor chip was implemented by the synthesis reaction of the AuNPs, which were charged positively through pH level adjustment, onto a negatively-charged cellulose substrate with ζ=–30.7 mV. The zeta potential, nanostructural properties, nanocrystallinity, and computational calculation-based electric field distributions of the cellulose-originated AuNPs were optimized to maximize LSPR phenomena and then characterized. Additionally, the performance of the SERS biosensor was compared under two representative excitation laser sources in the visible region (532 nm) and near-infrared region (785 nm). The Raman activities of our SERS biosensor chip were evaluated by trace small molecules (crystal violet, 2 μL), and the biosensor achieved an enhancement factor of 3.29×10^9 for the analytic concept with an excellent reproducibility of 8.5% relative standard deviation and a detection limit of 0.74 pM. Furthermore, the experimental results revealed that the five proposed SERS-based biomarkers could provide important information for identifying and predicting SAH-induced cerebral vasospasm and hydrocephalus complications (91.1% reliability and 19.3% reproducibility). Therefore, this facile and effective principle of our SERS biosensor chip may inspire the basis and strategies for the development of sensing platforms to predict critical complications in various neurosurgical diagnoses.

Graphical Abstract

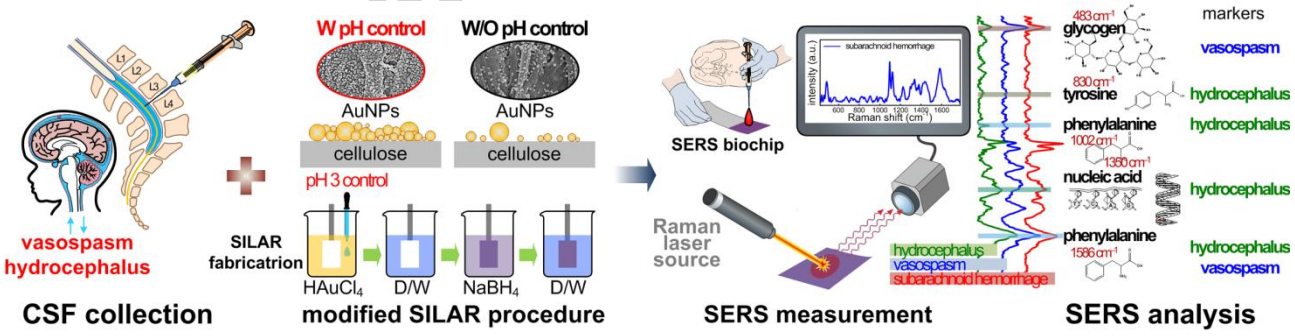

Keywords: surface-enhanced Raman spectroscopy, pH-adjusted cellulose strip, SERS biosensor, gold

nanoparticles, cerebrospinal fluid, subarachnoid hemorrhage

1. Introduction

Spontaneous subarachnoid hemorrhage (SAH) is a less common type of hemorrhagic stroke, caused by rupture of a cerebral aneurysm. It occurs in about one per 10,000 people every year and its mortality can reach 50% (Long et al., 2017). Some patients with SAH can recover almost all of their mental and physical functions, but most SAH incidents are accompanied by rebleeding, vasospasm, hydrocephalus, and other complications (Suarez et al., 2006). Rebleeding and vasospasm can be prevented by surgical clipping or endovascular coil embolization, while hydrocephalus can be treated by shunt surgery, endoscopic third ventriculostomy, and normal pressure hydrocephalus (Li et al., 2013; Ryttlefors et al., 2008; Sehba et al., 2012). Also, cerebral vasospasm can be treated by a medication called nimodipine. Cerebrospinal fluid (CSF) is the medium of the brain and spinal cord, containing water, numerous chemicals, and amino acids, and plays a critical role in the maintenance of neural structures. Since most cerebral aneurysms are located in the subarachnoid space, which is filled with CSF, an SAH typically causes dramatic changes in cerebral morphologies and properties, so CSF can be used as a potential biomarker in the prognosis of SAH. Fortunately, CSF samples can be easily obtained from external ventricular drainage or lumbar draining in SAH patients (van Gijn and Rinkel, 2001). Although many studies have been performed to find CSF biomarkers for classifying and predicting complications of SAH, particularly vasospasm or hydrocephalus, this procedure has not yet been established.

Raman spectroscopy is an optical spectroscopic technique based on inelastic scattering, defined by the difference in energy between incident photons and vibrational molecules. Most biological molecules have unique spectra, so that the biochemical compositions of complex biological specimens can be determined from their Raman signals (Ma et al., 2017a, 2017b; Xu et al., 2016; Zhao et al., 2017). However, since the energy involved in Raman scattering is extremely weak, many researchers have developed surface-enhanced Raman spectroscopy (SERS) platforms to amplify these signals (Wang et al., 2013; Yuan et al., 2017). The basic mechanism of SERS is that the signals of the analyte are amplified through the localized surface plasmon resonance (LSPR) phenomenon generated by light (Shiohara et al., 2014; Tong et al., 2014) when it interacts with plasmonic metal nanoparticles such as silver and gold (Wei et al., 2015). However, these SERS platforms are not likely to be appropriate for cost-effective mass production to apply point-of-care diagnostics (Wang et al., 2017).

Cellulose fibers have played important roles in various areas of human civilization, such as textiles, ropes, woven products, and other articles. These fibers are also used as litmus paper for pH indication and, in recent years, used in various applications, such as displays, batteries, and sensors (Ahmed et al., 2016; Lee et al., 2016; Nogi et al., 2009; Nyholm et al., 2011). This cellulose fiber-based platform is low-cost, mass-producible, disposable, biodegradable, easy to fabricate, and easy to use (Yetisen et al., 2013). Also, the surface of the cellulose platform is easily accessible,

and its hydrophilicity can be modifid by graft polymerization techniques and the covalent bonding of fatty acids, silanes, and other functional molecules (Missoum et al., 2013).

In this work, we introduce our strategy and implementation for improvement of the gold nanoparticle (AuNP)-enhanced LSPR effects by functionalization of the pH-adjusted cellulose surface and the possibility of its application to neurosurgical diagnosis (Scheme 1). The low concentrations of human CSF collected from the lumbar drainage system were analyzed by our pH-adjusted cellulose SERS biosensor with improved SERS performance by adding a stage in which pH was adjusted to 3 to the successive ionic layer adsorption and reaction (SILAR) fabrication procedure developed in our previous studies (Kim et al., 2017b, 2016, 2015). This pH level was determined by finding the pH of the most negatively charged cellulose fibers. Since this condition leads to strong absorption of a positively charged reactive nanoparticle seed ion (Au^{+}), the nanoparticles become uniformly and densely distributed over the cellulose substrate, and this functionalization will create a nanostructure optimized for LSPR effects. Multi-modal assessments to characterize the nanostructural properties and SERS performance of our cellulose-based SERS biosensor were performed in this study, such as the characterizations of zeta potential, nanostructural distribution and property, absorption property, sensitivity, relative standard deviation (RSD), SERS enhancement factor (EF), and the limit of detection (LOD). Furthermore, experimental and computational studies for selecting an incident Raman laser source for the AuNP-specialized paper strip biosensor were first considered.

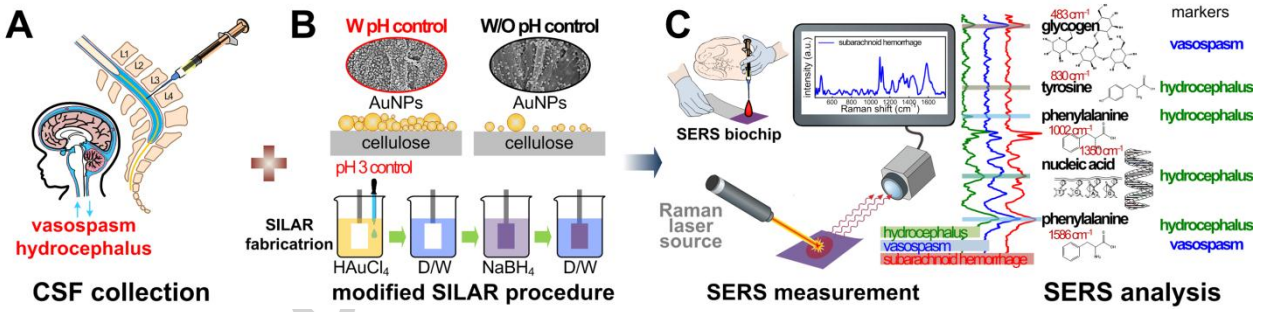

Scheme 1. A novel pH-adjusted cellulose SERS biosensor to detect the development of vasospasm and hydrocephalus after SAH from human CSF. (A) Collection of human CSF. (B) Development of a novel SERS cellulose strip with improved SERS performance through pH level adjustment during SILAR fabrication. (C) The general concept of this platform; we can predict the complication after SAH through rapid label-free diagnosis of human CSF extracted for clinical diagnosis.

2. Experimental section

2.1. Reagents and materials

Gold (III) chloride trihydrate ($HAuCl_4$, >99.9%) and sodium borohydride ($NaBH_4$, >96%) were purchased from Sigma Aldrich (St. Louis, MO, USA). Hydrochloric acid (HCl, >35%) and sodium hydroxide (NaOH, >95%) were

purchased from Duksan Pure Chemicals (Ansan, Korea). All reagents were of analytical grade, and all solutions were prepared using 18.3 $M\Omega \cdot cm^{-1}$ distilled water. Whatman cellulose chromatography paper from GE Healthcare (Cardiff, UK) was used as a substrate.

2.2. Fabrication

AuNPs were directly synthesized and coated on the cellulose strip using the SILAR technique modified from our previous study (Kim et al., 2016). The acidity of a gold salt agent ($HAuCl_4$) was pre-adjusted to pH levels 1– 7 using HCl and NaOH. Bare cellulose strips were treated with a 10 mM pre-adjusted $HAuCl_4$ agent and rinsed with distilled water. Then, they were treated with a 10 mM $NaBH_4$ reducing agent (pH 9.75) and rinsed again to wash away residues. Each pH-adjusted cellulose strip was successively immersed for 30 s in each solution and then subjected to five SILAR cycles.

2.3. Collection of CSF

CSF was obtained by a lumbar drainage system, which was performed for purely therapeutic purposes in patients with SAH, hydrocephalus, and central nervous system infection. Lumbar drainage was performed with a Hermetic™ Lumbar Drainage Accessory kit (Integra Neurosciences, Plainsboro, NJ, USA) with a 14 G Tuohy needle (9 cm) and an 80 cm Hermetic lumbar drainage catheter (0.7 mm ID, 1.5 mm OD), and the catheter was maintained for one week. The CSF drained at 5–10 cc/h, as determined by each individual's pathologic condition. The majority of as-prepared CSF was normally discarded, except for a small amount used for laboratory examination, e.g., chemical tests such as protein, glucose, and chloride levels and cell counts such as red blood cells, white blood cells, and their differential counts, which indicated the pathologic conditions of the patients. The CSF (<3 cc) used for Raman spectroscopy was frozen immediately and stored at –20°C. The retention period was not longer than one week. This prospective study was conducted at Kyung Hee University Hospital, South Korea. The participants provided informed consent for all procedures and for inclusion in the present study. The protocol was approved by the institutional review board of Kyung Hee University Hospital, South Korea (KHUH 2018-01-096-003).

2.4. Characterization

The zeta potential of the pH-adjusted cellulose fibers was characterized using a Zetatrac analyzer (Microtrac, Montgomeryville, PA, USA). Bare cellulose strips in distilled water were pulverized by 30 m of sonication, and then the pH levels of the suspensions were adjusted by HCl and NaOH solutions. All background surface charge values were calibrated with the same pH-adjusted distilled water. The distribution of the AuNPs synthesized onto the cellulose strip

was characterized using an S-4700 field emission scanning electron microscope (FE-SEM; Hitachi, Tokyo, Japan) at an accelerating voltage of 10 kV. The electron analysis of the AuNPs was characterized using a JEM-2100F field emission transmission electron microscope (FE-TEM; JEOL, Tokyo, Japan) at 200 kV. The ultraviolet-visible (UV–Vis) absorption of SILAR-synthesized AuNPs isolated from pH-adjusted cellulose strips was characterized using a T60U UV–Vis spectrophotometer (PG Instruments, Lutterworth, UK) with a 1-cm quartz cell at a scan rate of 0.4 nm. Ten milligrams of cellulose strips with the AuNPs in 5 mL of distilled water was sonicated for 30 m. Pure AuNPs were filtered by a sterile syringe filter with a 0.22-μm pore size hydrophilic polyethersulfone membrane (Millex®-GP, Merck Millipore, Germany). The crystalline phase of the AuNPs on silicon wafers was characterized using an ATX-G high resolution X-ray diffractometer (HR-XRD; Rigaku, Tokyo, Japan) with Cu Kα X-rays in the 2θ range of 30° to 80° with a step of 0.02°. The spectra of silicon in the range of 60° to 80° were eliminated to confirm the XRD patterns of the nanoparticles.

2.5. Raman spectra

Raman spectra were measured using a LabRam ARAMIS confocal Raman system (HORIBA Jobin Yvon, Lille, France). Two excitation sources, a 532-nm-line Ar-ion laser and a 785-nm-line diode laser, were used. Raman scattered light signals were collected using a 20× objective lens (N.A.=0.4). The optical power of the Raman laser was detected using a PM160 Portable Power Meter (ThorLabs, Newton, NJ, USA), and the beam intensities at the sample surface were appropriately modified by polarized filter. The spectrum of each measurement was recorded in the fingerprint range of 500–1750 cm^{-1} with an acquisition time of 10 s (×2) and two spectral resolutions of 1.5 cm^{-1} (the 532 nm laser) and 5 cm^{-1} (the 785 nm laser). The instrument was calibrated with a silicon wafer at the 520 cm^{-1} band. To ensure the reliability of the Raman spectra with trace samples, an average of 10 random spots on the SERS-active area for only a 2 μL droplet of analyte was used as a representative Raman spectrum.

2.6. Numerical analysis

The SERS effect of the pH-adjusted cellulose strip sensor was theoretically evaluated using the finite element method (FEM). The FEM computational model was designed based on information about the nanostructure of the pH-adjusted cellulose strip. The electric field distributions of a gold dimer were analyzed at two excitation wavelengths. The electric field values were represented as the maximum value of each computation. Three boundary conditions were used, including an active port boundary (for an incident wavelength boundary with laser power) and a passive port boundary (for a bottom boundary that does not pass reflections). The Floquet boundary condition was also imposed on both sides to provide an electric field with a symmetrical parallel boundary in the analytical models. The maximum and

minimum finite element sizes for computational analysis were set at 1 nm and 0.002 nm, respectively. The material properties for FEM analytical models were selected from the literature (Johnson and Christy, 1972; Kim et al., 2017a). The refractive index of air was 1.00029, and those of gold at 532 nm and 785 nm were 0.54386 and 0.14891, respectively. The complex-valued permittivity of gold was –4.68+2.43*i* and –22.86+1.42*i* at 532 and 785 nm, respectively. This computational calculation was performed in the radiofrequency module of the COMSOL software.

3. Results and discussion

3.1. Fabrication of pH 3-adjusted cellulose strips

To guarantee the performance of cellulose substrate-based Raman scattering sensing, various endeavors have been performed by our research groups (Kim et al., 2017b, 2016, 2015). Most substrates have been optimized in their intact state without additional chemical treatments. However, this process resulted in low formulation stability and lifetime. Surface charge is one of the most important properties affecting the performance of nanoparticle-based optical sensing devices (Fröhlich, 2012). Therefore, we aimed to develop a highly stable optical sensing device with SERS-optimized nanoparticles by controlling the surface charge of the cellulose substrate. Zeta potential (ξ) is the electric property between the solid and liquid interfaces with charge interaction. Although it does not exactly correspond with the surface charge of a material, it is still widely used for quantification of net surface charge. In this paper, the zeta potential of colloidal cellulose fibers was assumed to be the surface charge of the cellulose substrate.

Figure 1A shows the variations in zeta potential of cellulose fibers and the Raman intensities of crystal violet (CV) molecules using the cellulose substrates with SILAR-synthesized AuNPs at different pH levels. The zeta potential of pH 3-adjusted cellulose fibers showed the lowest negative electric potential (ξ=–30.7 mV), while those of cellulose fibers at other pH levels showed a slightly negative electric potential (ξ=–2.0±4.4 mV). Cellulose $(C_6H_{10}O_5)_n$ is a polysaccharide consisting of a linear chain of numerous D-glucose units. The pH of electrical charges on the surface of a polysaccharide depends on the pK_a of their ionizable side groups. The most common anionic side groups on polysaccharides are carboxylate groups, COO^- ($pK_a \approx 2.5-4.5$) (Ridley et al., 2001). Polysaccharides containing carboxyl groups are slightly acidic, so the chemical compound of cellulose fibers is expected to have a slightly negative potential. A carboxylate polysaccharide becomes deprotonated at pH levels higher than its pK_a (de Kruif and Tuinier, 2001). Furthermore, the absolute value of zeta potential for hydrophilic fibers decreases with increasing water adsorption caused by expansion of the bulk layer (Bellmann et al., 2005; Bismarck et al., 2002). These cellulose fibers containing acidic surface groups are completely dissociated in the additional alkaline. Therefore, the surfaces of cellulose fibers around a pH level of 3 had a strong negative charge, and a plateau in zeta potential above a pH level of 5 was observed (Reischl et al., 2006).

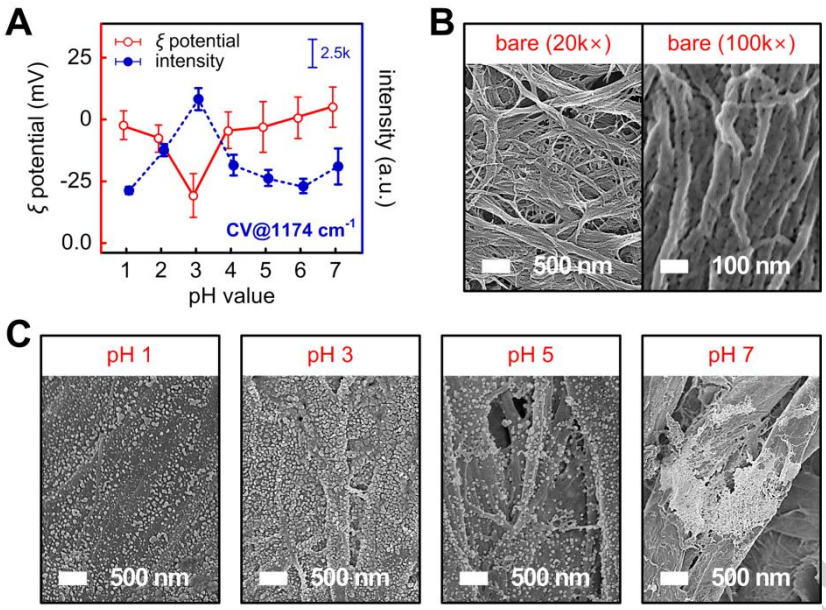

Figure 1. (A) Variations in zeta potential (ξ) of cellulose fibers and Raman intensities of CV using cellulose substrates adjusted to different pH levels (1–7). CV, crystal violet. (B) SEM images of bare cellulose substrate. (C) SEM images of distributions of the AuNPs synthesized by the SILAR procedure with different pH values of $HAuCl_4$ solution.

Based on the expectation that a positively charged reactive nanoparticle seed ion (Au^+) is likely to be strongly absorbed onto the surface of a negatively charged cellulose substrate (Figure 1B), the AuNP-synthesized cellulose substrates were fabricated with different pH levels of 1–7 (Figure 1C), which was determined to adjust pH level of $HAuCl_4$ solution, an AuNP seeding material in the SILAR fabrication procedure. At pH 3, the most uniform and dense distribution of AuNPs on a cellulose substrate was observed compared to other pH levels. The presence of aggregated and thinly deposited AuNPs was observed with increasing pH level. Intuitively, pH 3-adjusted cellulose substrate was likely to be the best for the LSPR in terms of the interparticle gap (Ding et al., 2017); experimentally, it showed the greatest Raman intensity compared to other pH levels (Figure 1A). SERS activity was evaluated using a droplet of 1 mM CV as a Raman trace molecule having three prominent Raman peaks at 1174 cm^{-1} (ring C– H bonding, representative CV molecule), 1390 cm^{-1} (N-phenyl stretching), and 1617 cm^{-1} (ring C– C stretching) (Zhang et al., 2011). Therefore, the negatively charged nature of the cellulose surface may be highly preferable for adsorption of positively charged Au^+ ions and can be synthesized directly by SILAR fabrication.

3.2. Characterization of plasmonic AuNPs

The positively charged SILAR-synthesized gold ions attached to negatively charged cellulose fibers were quantitatively determined by absorption in the UV–Vis spectral region. The UV–Vis spectra of the AuNPs isolated from cellulose fibers showed maximum absorption at a wavelength of 545 nm (Figure 2A). The number of SILAR-synthesized AuNPs increased slightly with increasing pH level up to pH 5. Generally, the pH level of reactants when synthesizing AuNPs in colloids directly affects the stabilizers or surfactants, such as poly(vinylpyrrolidone) or cetyltrimethylammonium bromide, and they in turn determine the size and shape of the nanoparticles (Chen et al., 2008; Chen et al., 2007). However, in this study, no difference in the absorption spectra of the AuNPs synthesized with different pH levels was observed. This result was responsible for the direct seeding of the nanoparticles without using stabilizers or surfactants. Therefore, pH level is likely to affect the functionalized substrate rather than the structure of the nanoparticles.

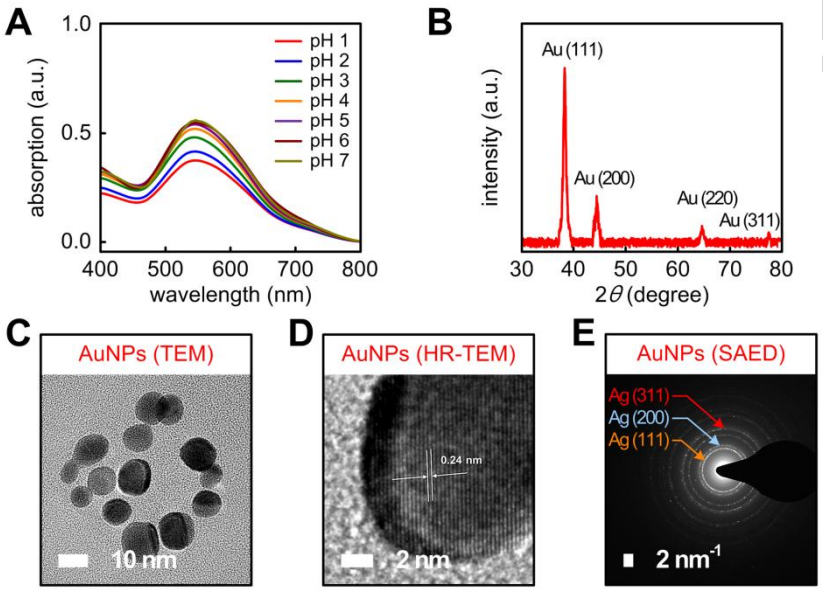

Figure 2. (A) UV-Vis absorption spectra of the AuNPs synthesized at different pH levels. (B) XRD pattern, (C) TEM image, (D) HR-TEM image, and (E) selected area electron diffraction (SAED) pattern of SILAR-synthesized plasmonic AuNPs synthesized at pH 3.

The plasmonic nanostructure of the SILAR-synthesized AuNPs was characterized by TEM, HR-TEM, selected area electron diffraction (SAED) and XRD assessments. Figure 2C shows the TEM image of the AuNPs, which were SILAR-synthesized at pH level 3, with an average size of about 10– 20 nm. An HR-TEM image (Figure 2D) with fringes of 0.24 nm *d*-spacing showed preferential growth of the AuNPs along the Au(111) plane. The SAED pattern of the AuNPs (Figure 2E) with several bright circular fringes along the Au(111), Au(200), and Au(311) planes showed highly polycrystalline gold (JCPDS No. 04-0784). XRD analysis of the AuNPs confirmed the mean positions of the

atoms in the crystal of nanoparticles by rapid ionic synthesis (Figure 2B). The prominent peaks of the AuNPs were observed at 2θ=38.1°, 44.4°, and 77.7°, indexed as Au(111), Au(200), and Au(311) diffractions, respectively. The XRD pattern of the AuNPs was consistent with the SAED finding. Therefore, this agreement suggested that the synthesized plasmonic AuNPs had a highly crystalline structure despite the ionic reaction of SILAR fabrication.

3.3. SERS performance

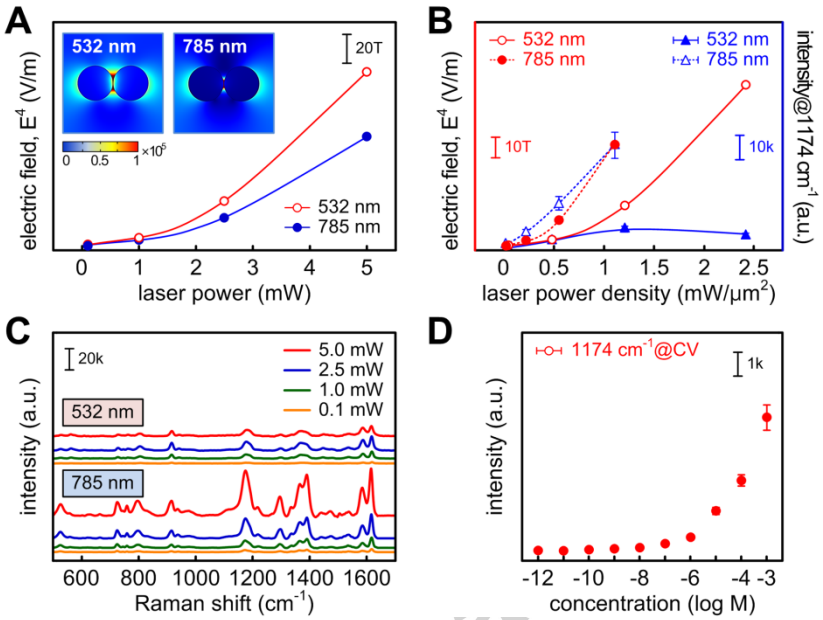

Figure 3. (A) Computational results of electric field distribution for a gold dimer with laser powers at two excitation wavelengths of 532 nm and 785 nm. (B) Variations in electric fields and Raman intensities of 1 mM CV at 1174 cm^{-1}, with laser power densities at two excitation wavelengths. (C) Raman spectra of 1 mM CV with laser powers at two excitation wavelengths. (D) Plot of Raman intensities at 1174 cm^{-1} with different CV concentrations.

To evaluate the effects of incident laser wavelengths on SERS application using our pH-adjusted cellulose strip sensor, Raman performance with two excitation wavelengths representing the visible region (532 nm) and near-infrared (NIR) region (785 nm) was investigated. This evaluation was motivated by the following: the intensity of Raman scattering is theoretically proportional to the fourth power of source energy (E^4), so that Raman signals generated by short wavelengths are more intense than those generated by long wavelengths at the same laser energy. At first, the electric field distributions with excitation wavelengths were investigated by a gold dimer model based on the optimized synthesis conditions for the AuNPs (Figure 3A) and more practical model extracted from the SEM image (Supplemental Information, Figure S1). The electric fields increased exponentially as the laser power increased, regardless of wavelength, and a shorter wavelength led to higher electric field distribution. A visible excitation wavelength laser is favorably used for analyzing various inorganic or mineral materials, while its use for organic

samples can result in some problems, such as the presence of highly fluorescent components and decreased sensitivity (Yang et al., 2012). Fluorescence can be suppressed or eliminated by selection of a longer 785 nm excitation wavelength. Furthermore, since a short wavelength or higher incident energy can damage an analyte composed of a soft substance, the choice of Raman excitation wavelengths is limited based on the application (Sivapalan et al., 2013; Zhang et al., 2018).

Raman laser powers in the range of 0.1– 5 mW were properly controlled by the manipulation of filters; however, since focal spot sizes differed, power density per unit area was used to compare Raman intensities with excitation wavelengths (Table S1). The electric fields increased exponentially with increasing laser power density regardless of wavelength, and a longer wavelength led to higher electric field distribution (Figure 3B, red curves). Interestingly, this computational finding was consistent with the experimental finding that a longer wavelength (785 nm) led to higher Raman intensities (1 mM CV at 1174 cm^{-1} representative peak), which increased exponentially with increasing laser power density (Figure 3B, blue curves). However, the Raman intensities at a 532 nm excitation wavelength showed degradation at power densities >0.5 $mW/\mu m^2$. Based on this, at the same power density (energy), it is natural that the Raman intensity of a 532 nm excitation wavelength should be about four to five times larger than that of a 785 nm excitation wavelength. However, the actual SERS effect of a 532 nm source laser did not demonstrate this effect; furthermore, it was decreased at power densities >1 $mW/\mu m^2$. This result is due to the damage of the cellulose fibers due to stronger energy and deeper penetration by the short wavelength energy. Some studies reported that the wavelengths of 500– 600 nm were less absorbent and reflective to cellulose components, and the cellulose fraction in wood underwent free radical-mediated partial degradation upon exposure to light (Andrady and Torikai, 1999; Kaczmarek et al., 2005). Figure 3C shows the SERS spectra of the Raman probe molecule CV with laser source powers. Although the synthesized AuNPs had higher absorption in the region near 550 nm (Figure 2A), a superior SERS effect was observed with a 785 nm source laser compared to a 532 nm source laser. Therefore, this result suggests that a NIR-wavelength excitation laser source is suitable for cellulose substrate-based SERS applications using biosamples.

The SERS performance of our pH-adjusted cellulose strip sensor was evaluated through sensitivity, RSD, EF, and LOD (signal-to-noise ratio>3). The cellulose SERS biosensor achieved a sensitivity with a correlation coefficient of 0.93 within the range of 1 pM to 1 mM for CV (Figure 3D), and the reproducibility was 8.5% RSD. The EF at 785 nm excitation wavelength calculated by the equation under similar conditions (Le Ru et al., 2007) was 3.29×10^9 for analytical chemistry and 2.25×10^7 for SERS substrate, where I_{SERS} and I_{bare} were the Raman intensities of a SERS cellulose strip (I_{SERS}=31.9) and bare cellulose substrate (I_{bare}=9.7), respectively, at the 1174 cm^{-1} peak (Table S2). The EF at 532 nm excitation wavelength was 4.09×10^6 for analytical chemistry and 2.79×10^2 for substrate. Although low concentrations of CV were applied to the cellulose SERS biosensor (Figure S2), SERS spectra with clear characteristic

peaks at 1174, 1390, and 1617 cm^{-1} were observed (LOD=0.74 pM). Therefore, a pH 3-adjusted, SILAR-synthesized AuNP-deposited SERS biosensor is expected to achieve excellent performance for SERS applications of biosamples.

3.4. Clinical applications

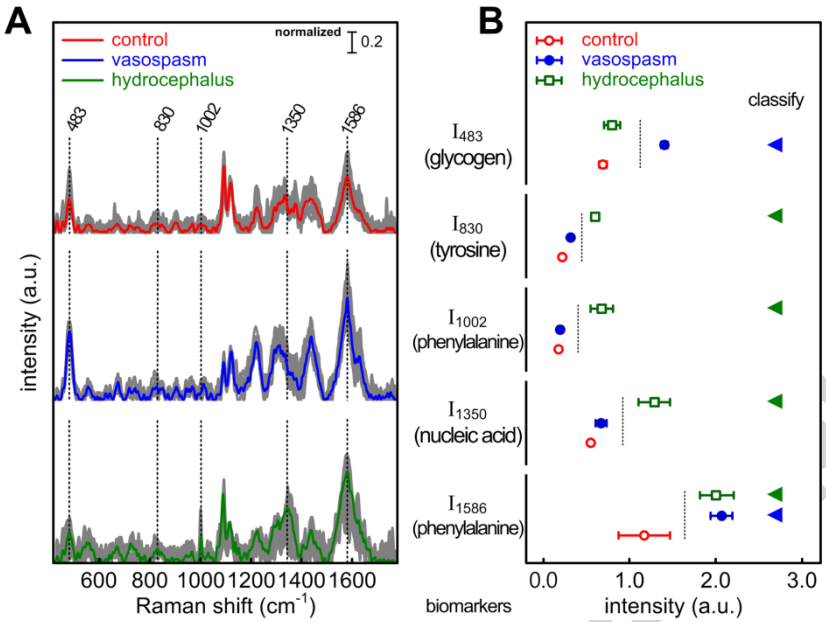

Figure 4. (A) Representative Raman spectra of control, cerebral vasospasm, and hydrocephalus groups measured using pH-adjusted SERS biosensors. (B) Five threshold-determined biomarkers with dominant Raman intensities, proposed for the early detection of vasospasm or hydrocephalus development after SAH.

The feasibility of our cellulose SERS biosensor was evaluated using human CSF after SAH; our SERS biosensor would provide information regarding the possibility of cerebral vasospasm or hydrocephalus development after SAH. Figure 4A shows the SERS signals of three CSF groups, the SAH (control, n=4), cerebral vasospasm (n=4), and hydrocephalus (n=4) groups, using the developed cellulose SERS biosensors. Since the concentration of each human CSF was different, each spectrum was normalized to the intensity of the 1120 cm^{-1} peak (C–O–C symmetric stretching) assigned to the cellulose. The dominant Raman peaks of the pH-adjusted SERS biosensor-detected CSF were detected at 483 cm^{-1} (glycogen), 830 cm^{-1} (tyrosine), 1002 cm^{-1} (phenylalanine), 1350 cm^{-1} (nucleic acids), and 1586 cm^{-1} (phenylalanine). Interestingly, all CSF Raman signals showed prominent peaks around 1095 and 1120 cm^{-1}, assigned to the C–H stretching indicative of cellulose (Lee et al., 2016). In general, since these peaks were not enhanced by the AuNPs, in most cases they were covered by high-concentration analytes. Thus, the presence of cellulose peaks indicates that the concentration of human CSF was very small (Figure S1). Although the human CSF would be at low concentrations, each pH-adjusted SERS biosensor-detected CSF Raman signal showed distinct morphological patterns

according to the acute disease developed after SAH (Figure 4A). Therefore, for early detection of SAH-induced cerebral vasospasm and hydrocephalus using human CSF, we proposed five threshold value (THV)-based biomarkers, i.e., I_{483}, I_{830}, I_{1002}, I_{1350}, and I_{1586}, corresponding to five dominant SERS peaks at 483, 830, 1002, 1350, and 1586 cm^{-1}, respectively (Figure 4B).

The increase in SERS intensities of the vasospasm group compared to the other groups at 483 cm^{-1} might be due to an increase in glycogen (I_{483}) (Konorov et al., 2011). Glycogen plays a role as the local energy buffer of glucose (Vander Heiden et al., 2009), which provides the energy source for physiological functioning of the brain through the generation of adenosine triphosphate (Mergenthaler et al., 2013). A serine-threonine kinase (Akt) is activated through the cell death and survival pathway in brain injury. The Akt activity in the acute phase of SAH inhibits the release of glycogen synthase kinase-3β through phosphorylation (Endo et al., 2006). Thus, glycogen stores are degraded after SAH, and this degradation may trigger the release of glucose during the development of cerebral vasospasm (Sakowitz et al., 2001; Vander Heiden et al., 2009). The increases in SERS intensities of the hydrocephalus group compared to the control at (1002 and 1586 cm^{-1}) and 830 cm^{-1} might be attributable to the increases in phenylalanine and tyrosine, respectively (Hernández et al., 2013). In particular, the hydrocephalus group showed significant increases in the SERS intensities at 1002 cm^{-1} compared to the others. The essential amino acid phenylalanine (I_{1002} and I_{1586}) converts to tyrosine, which is a precursor of the neurotransmitter dopamine. High levels of phenylalanine can damage the brain and cause severe intellectual disability. It is not yet known whether phenylalanine is a clear biomarker associated with hydrocephalus; however, to prevent hydrocephalus malformations in newborns, it is recommended that pregnant women eat less phenylalanine (Anderson et al., 2002). Tyrosine (I_{830}), which is synthesized from the phenylalanine, has been reported to have a profound effect on hydrocephalus (Goto et al., 2008). Also, some studies have reported markedly increased protein phenylalanine and tyrosine residues in the CSFs of patients with cerebral vasospasm after SAH (Provencio et al., 2010). This finding was consistent with our biomarker I_{1586}, which showed an increase in SERS intensities for both hydrocephalus and vasospasm groups. The hydrocephalus group showed an increased SERS intensity at the 1350 cm^{-1} peak assigned to nucleic acids, and this was likely to be an increase in the nuclear-to-cytoplasmic ratio related with malignant cells (Kong et al., 2015). The proposed THV-determined biomarkers suggest that the development of cerebral vasospasm after SAH can be detected with the 483 cm^{-1} peak in the CSF Raman spectra, while the development of SAH-induced hydrocephalus can be detected with the 830, 1002, and 1350 cm^{-1} peaks in the CSF Raman spectra. SAH-induced vasospasm and hydrocephalus can be differentiated through a 1581 cm^{-1} peak in the CSF Raman spectra. The consistency of newly proposed biomarkers in clinical applications showed high reliability of 87–93% and good reproducibility of 11–29% RSD (Table S3). Therefore, the label-free optical cellulose biosensor showing large improvement of SERS activity by pH adjustment is useful for early detection of potential

complications after SAH using human cerebrospinal-induced biofluids at low concentrations.

4. Conclusions

We reported a novel label-free SERS biosensor with improvements in the nanoparticle-enhanced LSPR effects for early diagnosis of SAH-induced complications using human lumbar CSF samples. A strategy for improvement of SERS performance was implemented by controlling the pH level of a metal salt solution in the process of SILAR synthesis, and the optimal pH level was determined as that of the cellulose fibers with the most negatively charged property (zeta potential, ξ=–30.7 mV). The optimally synthesized plasmonic AuNPs with an average size of 10– 20 nm had a highly crystalline structure despite ionic reaction. They had higher absorption in the visible region; however, since the visible-wavelength excitation laser source (532 nm) caused some problems such as damage of organic samples, fluorescent interference, and deteriorated sensitivity, an NIR-wavelength excitation laser source (785 nm) might be more suitable for AuNP-functionalized paper strip-based SERS applications using biosamples. The performance of our cellulose-based SERS biosensor was demonstrated by achieving the EF to detect single molecules (LOD <1 pM) and attain high reproducibility (<10%). The practical applicability of our label-free SERS biosensor was demonstrated through its ability to classify human CSF from patients with cerebral vasospasm and hydrocephalus, complications that might arise after SAH (>87% reliability and mean 19.3% reproducibility). We anticipate that this biosensor can be extended for the prediction of other complications in various neurosurgical diagnoses.

Acknowledgements

This research was supported by the National Research Foundation of Korea (2017R1A2B4002765 and 2018R1C1B6005132) and the Ministry of Health & Welfare, Republic of Korea (HI14C2241).

Conflict of Interest

The authors declare no competing financial interests.

References

Ahmed, S., Bui, M.-P.N., Abbas, A., 2016. Biosens. Bioelectron. 77, 249–263.

Anderson, P., Northam, E., Jacobs, R., Mikiewicz, O., Anderson, V.A., 2002. Child Neuropsychol. 8, 231–240.

Andrady, A.L., Torikai, A., 1999. Photoyellowing of mechanical pulps. III. Polym. Degrad. Stab. 66, 317–322.

Bellmann, C., Caspari, A., Albrecht, V., Loan Doan, T.T., Mäder, E., Luxbacher, T., Kohl, R., 2005. Colloids Surfaces

A Physicochem. Eng. Asp. 267, 19–23.

Bismarck, A., Aranberri-Askargorta, I., Springer, J., Lampke, T., Wielage, B., Stamboulis, A., Shenderovich, I., Limbach, H.-H., 2002. Polym. Compos. 23, 872–894.

Chen, H., Kou, X., Yang, Z., Ni, W., Wang, J., 2008. Langmuir 24, 5233–5237.

Chen, Y., Wang, C., Ma, Z., Su, Z., 2007. Nanotechnology 18, 325602.

de Kruif, C.G., Tuinier, R., 2001. Food Hydrocoll. 15, 555–563.

Ding, S.-Y., You, E.-M., Tian, Z.-Q., Moskovits, M., 2017. Chem. Soc. Rev. 46, 4042–4076.

Endo, H., Nito, C., Kamada, H., Yu, F., Chan, P.H., 2006. Stroke 37, 2140–2146.

Fröhlich, E., 2012. Int. J. Nanomedicine 7, 5577–5591.

Goto, J., Tezuka, T., Nakazawa, T., Sagara, H., Yamamoto, T., 2008. Mol. Cell. Neurosci. 38, 203–212.

Hernández, B., Pflüger, F., Kruglik, S.G., Ghomi, M., 2013. J. Raman Spectrosc. 44, 827–833.

Johnson, P.B., Christy, R.W., 1972. Phys. Rev. B 6, 4370–4379.

Kaczmarek, H., Oldak, D., Malanowski, P., Chaberska, H., 2005. Polym. Degrad. Stab. 88, 189–198.

Kim, W., Kim, Y.-H., Park, H.-K., Choi, S., 2015. ACS Appl. Mater. Interfaces 7, 27910–27917.

Kim, W., Lee, J.-C., Choi, S., 2017a. Int. J. Precis. Eng. Manuf. Technol. 4, 221–226.

Kim, W., Lee, J.-C., Lee, G.-J., Park, H.-K., Lee, A., Choi, S., 2017b. Anal. Chem. 89, 6448−6454.

Kim, W., Lee, J.-C., Shin, J.-H., Jin, K.-H., Park, H.-K., Choi, S., 2016. Anal. Chem. 88, 5531–5537.

Kong, K., Kendall, C., Stone, N., Notingher, I., 2015. Adv. Drug Deliv. Rev. 89, 121–134.

Konorov, S.O., Schulze, H.G., Atkins, C.G., Piret, J.M., Aparicio, S.A., Turner, R.F.B., Blades, M.W., 2011. Anal. Chem. 83, 6254–6258.

Le Ru, E.C., Blackie, E., Meyer, M., Etchegoin, P.G., 2007. J. Phys. Chem. C 111, 13794–13803.

Lee, S.H., Ban, J.Y., Oh, C.-H., Park, H.-K., Choi, S., 2016. Sci. Rep. 6, 28588.

Li, H., Pan, R., Wang, H., Rong, X., Yin, Z., Milgrom, D.P., Shi, X., Tang, Y., Peng, Y., 2013. Stroke 44, 29–37.

Long, B., Koyfman, A., Runyon, M.S., 2017. Emerg. Med. Clin. North Am. 35, 803–824.

Ma, W., Fu, P., Sun, M., Xu, L., Kuang, H., Xu, C., 2017a. J. Am. Chem. Soc. 139, 11752–11759.

Ma, W., Sun, M., Fu, P., Li, S., Xu, L., Kuang, H., Xu, C., 2017b. Adv. Mater. 29, 1703410.

Mergenthaler, P., Lindauer, U., Dienel, G.A., Meisel, A., 2013. Trends Neurosci. 36, 587–597.

Missoum, K., Belgacem, M., Bras, J., 2013. Materials (Basel). 6, 1745–1766.

Nogi, M., Iwamoto, S., Nakagaito, A.N., Yano, H., 2009. Adv. Mater. 21, 1595–1598.

Nyholm, L., Nyström, G., Mihranyan, A., Strømme, M., 2011. Adv. Mater. 23, 3751–3769.

Provencio, J.J., Fu, X., Siu, A., Rasmussen, P.A., Hazen, S.L., Ransohoff, R.M., 2010. Neurocrit. Care 12, 244–251.

Reischl, M., Stana-Kleinschek, K., Ribitsch, V., 2006. Macromol. Symp. 244, 31–47.

Ridley, B.L., O'Neill, M.A., Mohnen, D., 2001. Phytochemistry 57, 929–967.

Ryttlefors, M., Enblad, P., Kerr, R.S.C., Molyneux, A.J., 2008. Stroke 39, 2720–2726.

Sakowitz, O.W., Wolfrum, S., Sarrafzadeh, A.S., Stover, J.F., Dreier, J.P., Dendorfer, A., Benndorf, G., Lanksch, W.R., Unterberg, A.W., 2001. J. Cereb. blood flow Metab. 21, 1067–1076.

Sehba, F.A., Hou, J., Pluta, R.M., Zhang, J.H., 2012. Prog. Neurobiol. 97, 14–37.

Shiohara, A., Wang, Y., Liz-Marzán, L.M., 2014. J. Photochem. Photobiol. C Photochem. Rev. 21, 2–25.

Sivapalan, S.T., DeVetter, B.M., Yang, T.K., van Dijk, T., Schulmerich, M. V, Carney, P.S., Bhargava, R., Murphy, C.J., 2013. ACS Nano 7, 2099–2105.

Suarez, J.I., Tarr, R.W., Selman, W.R., 2006. N. Engl. J. Med. 354, 387–396.

Tong, L., Xu, H., Käll, M., 2014. MRS Bull. 39, 163–168.

van Gijn, J., Rinkel, G.J.E., 2001. Brain 124, 249–278.

Vander Heiden, M.G., Cantley, L.C., Thompson, C.B., 2009. Science 324, 1029–1033.

Wang, Y., Yan, B., Chen, L., 2013. Chem. Rev. 113, 1391–1428.

Wang, Z., Zong, S., Wu, L., Zhu, D., Cui, Y., 2017. Chem. Rev. 117, 7910–7963.

Wei, H., Hossein Abtahi, S.M., Vikesland, P.J., 2015. Environ. Sci. Nano 2, 120–135.

Xu, L., Zhao, S., Ma, W., Wu, X., Li, S., Kuang, H., Wang, L., Xu, C., 2016. Adv. Funct. Mater. 26, 1602–1608.

Yang, W., Wu, H., Qian, J., Chandler, L., Lieber, C.A., Dentinger, C., 2012. Proc. SPIE; Opt. Photonics Counterterrorism, Crime Fight. Def. VIII 8546, 854603.

Yetisen, A.K., Akram, M.S., Lowe, C.R., 2013. Lab Chip 13, 2210–2251.

Yuan, Y., Panwar, N., Yap, S.H.K., Wu, Q., Zeng, S., Xu, J., Tjin, S.C., Song, J., Qu, J., Yong, K.-T., 2017. Coord. Chem. Rev. 337, 1–33.

Zhang, D., Huang, L., Liu, B., Ni, H., Sun, L., Su, E., Chen, H., Gu, Z., Zhao, X., 2018. Biosens. Bioelectron. 106, 204–211.

Zhang, L., Lang, X., Hirata, A., Chen, M., 2011. ACS Nano 5, 4407–4413.

Zhao, Y., Sun, M., Ma, W., Kuang, H., Xu, C., 2017. J. Phys. Chem. Lett. 8, 5633–5642.

Highlights

1. Bare cellulose at pH 3 showed the lowest negative electric potential, ζ=–30.7 mV.
2. A pH adjustment led to improved SERS performance of the cellulose biosensor chip.
3. Five SERS-based biomarkers were proposed to predict SAH-induced complications.